

Transport Properties of Active Particles Moving on Adjustable Networks

William G. C. Oropesa,^{1,2,*} Pablo de Castro,^{1,2} Hartmut Löwen,³ and Danilo B. Liarte^{1,2,4,†}

¹*Instituto de Física Teórica, UNESP – Universidade Estadual Paulista,
Rua Dr. Bento T. Ferraz 271, 01140-070, São Paulo, SP, Brazil*

²*ICTP South American Institute for Fundamental Research, São Paulo, SP, Brazil*

³*Institut für Theoretische Physik II: Weiche Materie,*

Heinrich-Heine-Universität Düsseldorf, Universitätsstr. 1, D-40225 Düsseldorf, Germany

⁴*Department of Physics, Cornell University, Ithaca, NY 14853, USA*

(Dated: February 5, 2026)

Active adaptive matter has attracted considerable interest due to its rich, largely unexplained dynamics and its relevance to a wide range of synthetic and biological materials. An important subclass of such systems consists of active particles that can remodel the network in which they move. Here, we introduce a minimal yet versatile model of active particles moving on an adjustable network. In this model, particles undergo discrete run-and-tumble motion along the links of a triangular lattice and leave behind a trail of temporarily blocked links. These closed links cannot be traversed by other particles and reopen only after a characteristic healing time. The resulting trail-mediated blocking mechanism is fundamentally distinct from more familiar interactions such as excluded-volume effects. In the high-persistence limit, we find a qualitative contrast between the two mechanisms: while steric blocking leads to reduced diffusivity with increasing persistence, trail-induced blocking causes diffusivity to increase monotonically. We characterize this fundamental difference and the associated, unexpected transport properties, and discuss potential applications of our findings.

I. INTRODUCTION

In recent years, a wide range of striking phenomena have been reported in connection with the unusual transport properties of active matter [1–8]. Many of these effects can be traced back to what is arguably the most ubiquitous feature of active matter systems: *persistent motion*. As a consequence of persistence, a single active particle undergoing stochastic motion remains in a super-diffusive regime for times up to the *persistence time*, defined as the average time over which the particle maintains its direction of motion [9, 10]. In interacting systems, persistence gives rise to even more remarkable behavior. Notably, it can drive spontaneous *agglomeration* or *clustering* even in systems with purely repulsive interactions [11–14]. In its most prominent manifestation, this mechanism leads to the well-known phenomenon of *motility-induced phase separation* (MIPS) [15–17]. Persistence also plays a crucial role in determining long-time transport properties. For instance, the diffusion coefficient of an active particle moving in a porous medium exhibits a nonmonotonic dependence on the persistence time: in the large-persistence limit, diffusion is suppressed due to persistence-induced accumulation at confining boundaries [18, 19]. Similarly, in systems of mutually repulsive active particles, the collective diffusion coefficient also displays a nonmonotonic dependence on persistence, primarily as a result of clustering [20–22]. Here we consider a more general setting in which particle motion actively induces topological changes in the

embedding medium — in our case a discrete network. We show that this coupling leads to a novel mechanism of diffusion suppression that is fundamentally distinct from the interaction-driven slowing down associated with agglomeration [23–27].

Network topology adjustment has emerged as a key mechanism underlying a wide range of phenomena in both synthetic [28] and biological materials. In vertex models of confluent cell tissues, changes in network topology provide the essential mechanism that enables cell rearrangements and mobility in the fluid-like regime [29, 30]. More generally, systematic bond removal in elastic networks—known as the tuning-by-pruning protocol—has been shown to regulate and optimize the mechanical response of diverse material systems [31–33]. This framework was subsequently extended to achieve localized, long-range, and controllable responses in elastic and flow networks [34, 35]. In this mechanical analogue of allosteric regulation, a localized strain (or pressure drop) applied at position \mathbf{r} induces a prescribed, spatially separated response at position \mathbf{r}' . More recently, networks with adaptable degrees of freedom have been equipped with local learning rules that enable them to modify their internal structure and optimize performance in response to sequences of external stimuli [36–39]. This line of work has employed the paradigm of physical learning [40], which has generated significant interest as a framework for understanding complex adaptive systems and for designing intelligent mechanical metamaterials.

Recently, there has been growing interest in the study of active particles moving within adaptable and dynamic media. For example, Jin et al. investigated the dynamics of self-propelled droplet swimmers that exhibit both chemotaxis and negative autochemotaxis [28]. As these

* oropesaw@ictp-saifr.org

† danilo.liarte@ictp-saifr.org

particles move, they deposit chemical trails that can either attract or repel other particles. These trails have a finite lifetime due to dispersion. Using microfluidic devices with bifurcating channels, the authors demonstrated anti-correlations in the branch choices of successive swimmers and showed how chemotactic responses can guide swimmers through a maze. Another example of the important interplay between active motion and the surrounding medium is provided by the migration of certain unicellular organisms, such as the slime mold *Physarum polycephalum*, on different substrates. Tröger et al. showed that, regardless of the presence or absence of food, these organisms achieve superdiffusive migration by performing self-avoiding run-and-tumble dynamics [41]. Finally, a further system of interest involves fibroblasts and other cell types migrating through the connective tissue of cartilage [42, 43]. As part of their role in tissue repair, fibroblasts are responsible for the production and maintenance of the extracellular matrix.

Here we introduce a minimal yet versatile model that explicitly couples active particle dynamics to the adaptive evolution of network topology. Specifically, we consider a system of active particles with density ϕ moving along the bonds of a regular triangular lattice [44]. Various phenomena in active matter have been described using a fixed underlying lattice [27, 45–48], but in our model the lattice topology changes dynamically. Particle motion follows a discrete run-and-tumble dynamics characterized by a persistence time τ_p . Crucially, particle trajectories actively modify the underlying network: when a particle traverses a bond b connecting two sites, that bond temporarily closes and becomes inaccessible to all particles, including the particle that created the closure. Each closed bond reopens after a characteristic healing time τ_h . Hence the particle motion occurs on an *adjustable network*. In addition to this trail-mediated interaction, particles experience excluded-volume constraints, such that no two particles may occupy the same lattice site. We demonstrate that these two blocking mechanisms—self-generated bond closures and mutual excluded-volume interactions—give rise to qualitatively distinct transport regimes. At long persistence times, excluded-volume interactions combined with directional persistence promote particle agglomeration, leading to a suppression of effective diffusion as persistence increases. By contrast, transport hindered by closed bonds exhibits the opposite trend: increasing persistence systematically enhances diffusion. The competition between these two fundamentally different blocking mechanisms underlies the nontrivial and counterintuitive dependence of transport properties on system parameters. In particular, we find that the optimal persistence time that maximizes diffusion (as a function of τ_p) decreases with increasing particle density, yet increases with the bond healing time. These results highlight how feedback between active motion and adjustable connectivity can qualitatively reshape transport in active systems.

The remainder of the paper is organized as follows.

Sections II and III describe the model and the numerical simulation methods, respectively. Section IV presents the results for both fixed network topologies (Section IV A) and adjustable network topologies (Section IV B). Concluding remarks are provided in Section V. Finally, Appendix A examines a variant of the model without excluded-volume interactions, in which multiple particles may occupy the same site.

II. NETWORK MODEL

We consider a regular triangular lattice with N sites connected by nearest-neighbor bonds between pairs (dark green lines in Fig. 1a). Each lattice site $i \in \{0, \dots, N-1\}$ has nearest neighbors located a lattice spacing away along z possible directions, which we label $\ell \in \{0, \dots, z-1\}$ ($z = 6$ for the triangular lattice). For future reference, we introduce a lattice index neighbor function $\varphi(i, \ell) \in \{0, \dots, N-1\}$, which indexes the nearest neighbor of i in the direction ℓ . In our model, each bond connecting nearest-neighbor sites can be either open or closed. This is described by a lattice degree of freedom $\kappa_{i\ell} \in \{0, 1\}$, which takes value 0 or 1 for closed and open bonds, respectively. Notice that this variable is redundant: For each site i and direction ℓ , there is a neighboring site $j = \varphi(i, \ell)$ so that $\kappa_{j\bar{\ell}} = \kappa_{i\ell}$, where $\bar{\ell} = (\ell + \lfloor z/2 \rfloor) \bmod z$ is the opposite direction to ℓ and $\lfloor \cdot \rfloor$ is the floor function.

Now we populate this lattice with a set of N_p ($\leq N$) active particles, so that each lattice site can be either empty or occupied by at most one particle. The state of site i is thus described by the occupation variable $\sigma_i \in \{0, 1\}$, where 0 and 1 denote empty and occupied sites, respectively. Alternatively, a configuration of active particles is described by two variables: (i) the coordinate $x_\alpha \in \{0, \dots, N-1\}$ giving the lattice site index for particle $\alpha \in \{0, \dots, N_p-1\}$ (henceforth we use greek and latin indexes for particle and lattice indexes, respectively); (ii) the direction of self-propulsion $n_\alpha \in \{0, \dots, z-1\}$ of particle α (represented by arrows in Fig. 1). A general configuration for the system is completely determined by the variables $\kappa_{i\ell}$, x_α and n_α , with $i \in \{1, \dots, N-1\}$, $\ell \in \{0, \dots, z-1\}$ and $\alpha \in \{0, \dots, N_p-1\}$. In this paper we consider periodic boundary conditions (PBCs).

The particles undergo a run-and-tumble dynamics, i.e., unless a particle α is blocked, it will move along its internal self-propulsion direction n_α . In turn, this direction can change at each time step Δt with probability $\alpha_p \Delta t$, where α_p is the tumbling rate. The tumbling rate determines a characteristic time scale, the persistence time $\tau_p = 1/\alpha_p$, giving the average time between consecutive tumbles. Note that for $\tau_p = \Delta t$, we recover the passive limit, where particles follow a traditional dynamics in which the director virtually changes at every time step. Conversely, for $\tau_p \rightarrow \infty$ we recover deterministic ballistic motion along a fixed direction with no tumbles. The

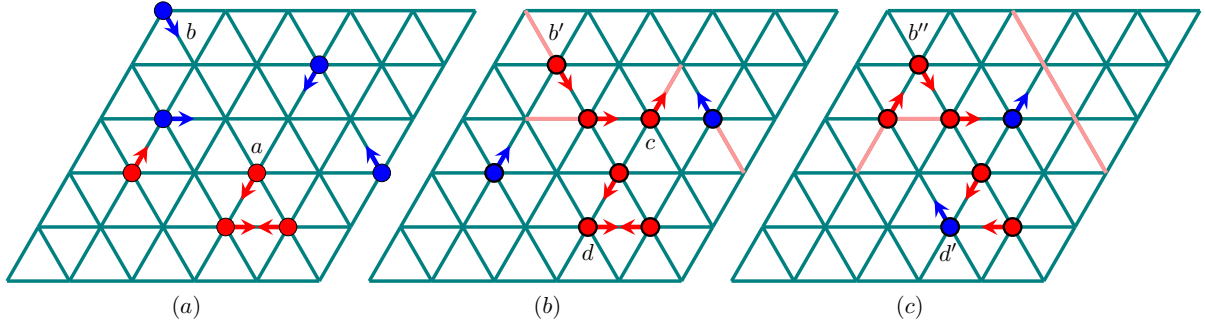


FIG. 1. Illustration of our network model. Run-and-tumble active particles are added to the nodes of a regular triangular lattice with nearest-neighbor connections. Blocked and moving particles are represented by red and blue disks, respectively. The arrows indicate the direction of self-propulsion. Light blue and yellow lines represent open and closed bonds, respectively. A particle d in (b) changes its configuration to d' in (c) by tumbling, i.e. changing its self-propulsion direction, with a rate $\alpha_p = 1/\tau_p$. An open bond b in (a) traversed by a particle has its configuration changed to a closed bond b' in (b). The closed bond b' in (b) can then spontaneously “heal” to an open bond state b'' in (c) with healing rate, $\alpha_h = 1/\tau_h$. A particle will be blocked either if it tries to move to an occupied site [a in (a)] or if it tries to move through a closed bond [c in (b)].

tumble process is schematically represented for particle $d \rightarrow d'$ in Figs. 1b and 1c.

Whenever a particle traverses a bond $\kappa_{i\nu}$, it becomes closed, i.e. $\kappa_{i\nu} \rightarrow 0$ (see bonds b and b' in Figs. 1a and 1b). Once closed, the bond can spontaneously “heal” and return to the open state ($\kappa_{i\nu} = 1$) at each time step with probability $\alpha_h \Delta t$, where α_h is the healing rate (see bonds b' and b'' in Figs. 1b and 1c). The healing rate determines another important characteristic time scale, the healing time $\tau_h = 1/\alpha_h$, which represents the average time for a closed bond to regenerate. The limit $\tau_h = \Delta t$ represents the case where bonds heal at every time step with certainty, effectively making the system behave as if all bonds were always open. Finally, a particle α with director n_α at site x_α will be blocked (i.e. not move) either if the intended neighboring site is occupied [$\sigma_{\varphi(x_\alpha, n_\alpha)} = 1$, see particle a in Fig. 1a] or if the intended crossing bond is closed [$\kappa_{x_\alpha n_\alpha} = 0$, see particle c in Fig. 1b].

The dynamic behavior of our system is controlled by three parameters: The persistence time τ_p , the healing time τ_h and the density of active particles $\phi = N_p/N$. Without loss of generality, we consider the velocity of the particles $u = a/\Delta t$ to be constant, where a is the lattice spacing.

III. NUMERICAL SIMULATIONS

In this section, we present details of our large-scale Monte Carlo simulations on modern GPUs. We consider triangular lattices of size $N = L \times L$, and PBCs. The number of particles $N_p = \phi N$ is determined by the size and packing fraction ϕ . All simulations were implemented in CUDA [49, 50], enabling efficient parallel updates of particle motion and bond dynamics. Here,

particle and lattice topology are simultaneously updated on the GPU, which allows us to simulate large lattices over long timescales with minimal computational overhead.

In all simulations, the initial network configuration is a complete triangular lattice, i.e. all bonds are open— $\kappa_{i\ell}(0) = 1$ for all i, ℓ . We then assign random values for the position and the director of each active particle α , which we draw from uniform distributions over the discrete sets of lattice sites and orientations, respectively. At each Monte Carlo step (MCS), the dynamics follows a two-stage protocol:

1. *Particle movement.* We update the state of each particle α with director n_α at site i in two steps. (a) The director changes with probability $\Delta t/\tau_p$ to a new direction uniformly distributed among the discrete z lattice directions. (b) The particle attempts to move to its neighboring site $j = \varphi(i, n_\alpha)$ along the direction of its current director. The move is accepted if the target site is empty ($\sigma_j = 0$) and the bond connecting the two sites is open ($\kappa_{in_\alpha} = 1$). If the move is successful, we exchange the occupancy variables σ_i and σ_j , and update the coordinate x_α , as well as the bond variable $\kappa_{in_\alpha} = 0$, indicating that that bond is now closed.
2. *Bond “healing”.* After all particle updates, each closed bond is allowed to ‘heal’. A closed bond will be open again with probability $\Delta t/\tau_h$. If the healing is successful, we update the bond variable $\kappa_{i\ell} = \kappa_{j\ell} = 1$ for $j = \varphi(i, \ell)$.

For each triplet of parameters (ϕ, τ_p, τ_h) , we first evolve the system for a total of $N_{\text{ther}} = 10^5$ MCSs. Then we run the simulations for another $N_{\text{step}} = 10^5$ MCSs to measure the various quantities of interest. We employ

independent realizations initialized with distinct random-number seeds to compute ensemble averages and estimate statistical uncertainties. The number of realizations depends on the particle density. For relatively low densities ($N_p \sim 2 \times 10^4$), we use 10 independent realizations, whereas for higher densities ($N_p \sim 3 \times 10^5$) we use 5 realizations. We have verified that these numbers of realizations are sufficient and lead to statistically stable averages.

We have used triangular lattices of linear size $L = 1024$, and the particle packing fraction was varied in the range $0.016 \leq \phi \leq 0.256$, which is well below the triangular-lattice site-percolation threshold $\phi_c = 1/2$ [51]. We also fixed the units for all simulations: the time step was set to $\Delta t = 1$ and the lattice constant to $a = 1$. Henceforth, unless stated otherwise, all times (including τ_h and τ_p) will be expressed in units of Δt , and all distances will be expressed in units of a . The diffusion coefficient is then expressed in units of $a^2/\Delta t$.

To mitigate finite-size artifacts associated with periodic boundaries, we have limited the persistence time τ_p so that particles do not travel distances comparable to the system linear size without reorienting. Without this constraint, particles could traverse the entire domain, wrap around the periodic box, and artificially interact with their own periodic images (particularly if τ_h is large), thereby generating spurious dynamical correlations. Hence, we have sampled the persistence time logarithmically within the interval $\tau_p \in [1, 1000]$. In turn, we have sampled the healing time (which does not introduce further comparable finite-size artifacts) logarithmically within the interval $\tau_h \in [1, 320]$.

IV. RESULTS

A. Fixed network topology ($\tau_h = 1$)

We first consider the case in which the network topology is fixed, with all bonds open throughout the simulation. This case can be more conveniently implemented by setting $\tau_h = 1$, so that closed bonds are healed (reopened) after each time step. The results of this section will provide a check, as there is a vast literature describing the dynamic behavior of run-and-tumble particles in two dimensions, both in the continuum [20] and in discrete lattices [22]. At fixed density, the effective diffusion coefficient is expected to linearly increase with τ_p at low persistence time ($D_{\text{eff}} \propto \tau_p$), reach a maximum (usually associated with the onset of clustering in the system), and finally decrease with τ_p as $D_{\text{eff}} \propto \tau_p^{-1}$ at high persistence time. As we shall discuss in the next paragraph, our results corroborate this picture. Also, we introduce additional measurements that shed light into the relation between clustering and optimal diffusion in these systems.

Figure 2a shows the effective diffusion coefficient D_{eff} as a function of persistence time τ_p , for different packing

fractions ϕ . As it should be anticipated, at fixed ϕ , D_{eff} linearly increases with τ_p at low τ_p , reaches a maximum at some optimal persistence time τ_p^* , and then decreases as τ_p^{-1} at high τ_p . This global behavior is well reproduced for a wide range of values of ϕ . As expected, an increase in ϕ leads to an overall decrease of D_{eff} , due to the repulsive interactions between particles. Besides, an increase in ϕ leads to a decrease of the optimal persistence time τ_p^* — higher density facilitates agglomeration, which is ultimately responsible for the decrease of D_{eff} at high τ_p .

To quantify agglomeration and clarify its connection to optimal persistence (even in phase-space regions sufficiently far away from MIPS), we calculate the fraction of particles located in the deep interior of a cluster,

$$\eta_{\text{int}} = \frac{\sum_{\alpha} \delta_{N_{\alpha}, z}}{\sum_{\alpha} \Theta(N_{\alpha})}, \quad N_{\alpha} = \sum_{\ell=1}^z \sigma_{\varphi(x_{\alpha, \ell})}. \quad (1)$$

Here N_{α} is the number of occupied nearest-neighbors of particle α , $\delta_{i,j}$ is the Kronecker delta, and Θ is the Heaviside function. For our triangular lattice model, this is just the number of particles with six neighbors divided by the number particles with at least one neighbor. Figure 2b shows that τ_p^* correlates very well with the value of τ_p marking the onset of a finite value of η_{int} . For instance, see the black dashed line connecting figures 2a and 2b: The optimal persistence time marks both the maximum of D_{eff} and (approximately) the onset of η_{int} for $\phi = 0.064$ (magenta triangles in the figure). Although the crossover to finite η_{int} is not sharp, this result provides a simple explanation for the agglomeration mechanism that is responsible for non-monotonic diffusion in these systems.

To illustrate the clustering mechanism responsible for optimal persistence and the subsequent decrease of diffusion at larger τ_p , Figs. 3a and 3b show snapshots of particle configurations in the lattice for $\phi = 0.064$, and $\tau_p = \tau_p^{(1)} = 10 < \tau_p^*$ (a), and $\tau_p = \tau_p^{(2)} = 100 > \tau_p^*$ (b). These snapshots show clearly that although there are small clusters already present in (a) $\tau_p < \tau_p^*$, only in (b) ($\tau_p > \tau_p^*$) one can see the formation of large clustered structures with a finite fraction of particles in the deep interior of a cluster.

We end this section with a brief discussion about the apparent invariant scaling behavior depicted in Fig. 2a. Notice that all curves seem to have same shape in a log-log scale, which suggests that D_{eff} follows a simple scaling form,

$$D_{\text{eff}} = \phi^{-\lambda} \mathcal{F}(\tau_p \phi^{\lambda}), \quad (2)$$

where λ is a scaling exponent, and \mathcal{F} is a scaling function. The fact that the scaling exponents for D_{eff} and τ_p are the same is a consequence of the linear regime at low persistence times. In fact, at low τ_p , Eq. (2) implies that $\mathcal{F}(x) \sim x$ at low x , so that $D_{\text{eff}} \sim \tau_p$ independent of ϕ . In turn, at high τ_p we must have $\mathcal{F}(x) \sim x^{-1}$, so that we can derive a simple estimate for τ_p^* from the condition,

$$f_- \phi^{-\lambda} \tau_p^* \phi^{\lambda} = f_+ \phi^{-\lambda} (\tau_p^* \phi^{\lambda})^{-1} \rightarrow \tau_p^* \sim \phi^{-\lambda}, \quad (3)$$

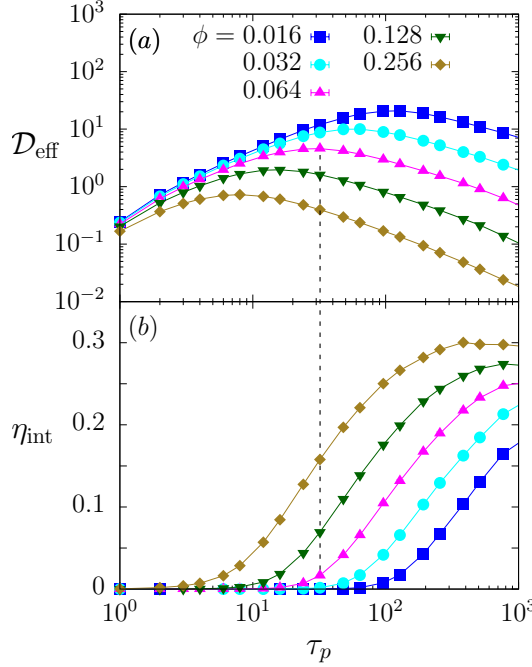


FIG. 2. (a) Effective diffusion coefficient as a function of persistence time for different packing fractions. (b) Fraction of particles in the deep interior of a cluster (particles surrounded by z other particles). The dashed vertical line indicates $\tau_p^* \approx 32$, corresponding to the maximum diffusion for the system with packing fraction $\phi = 0.064$ (magenta curve), as well as the onset of a finite population of particles in the interior of a cluster.

where f_- and f_+ are the power-law amplitudes of D_{eff} below and above the optimal persistence, respectively. Figure 4a shows a scaling collapse plot for re-scaled diffusion coefficient $D_{\text{eff}}\phi^\lambda$ as a function of rescaled persistence time $\tau_p\phi^\lambda$. The exponent $\lambda \approx 1$ is chosen to yield the best collapse of the data. Notice that the largest value of $\phi = 0.256$ lies outside the scaling regime, which should be primarily valid at small ϕ . Figure 4b shows a density plot of η_{int} as a function of density ϕ and persistence time τ_p . The white squares show the simulation results for $\tau_p^* = \tau_p^*(\phi)$ and solid red line shows the best fit using our theoretical prediction for $\tau_p^* \sim \phi^{-\lambda}$. Notice that there is excellent agreement between the direct calculation of τ_p^* , the onset of non-zero η_{int} and our theoretical prediction in Eq. (3).

B. Adjustable network topology ($\tau_h > 1$)

We now consider $\tau_h > 1$, i.e. the network topology changes due to particle motion. Now the healing time τ_h — the average time it takes for a closed bond to re-open — plays a fundamental role. The larger the value of τ_h , the larger the chance that a particle will be blocked by a closed track. Hence one would naively expect that

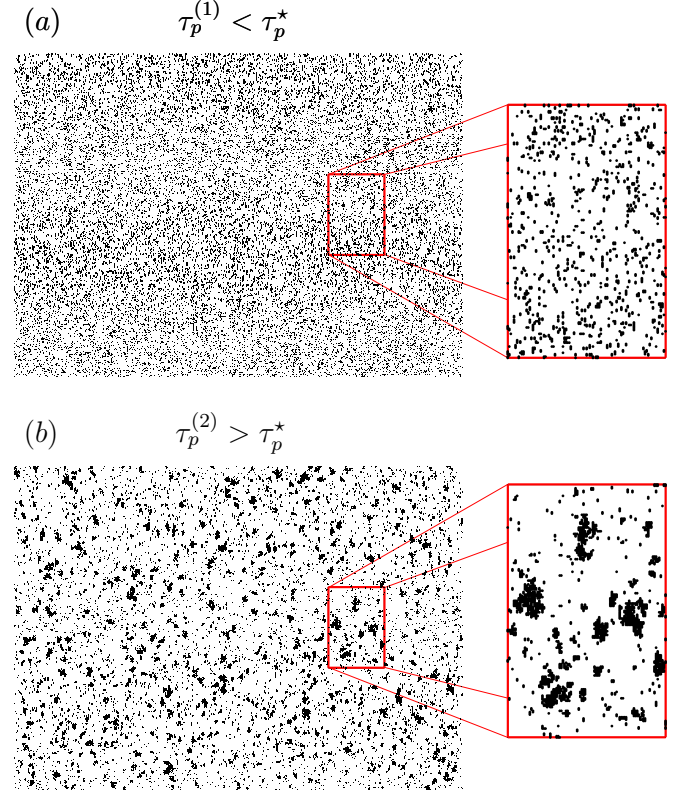


FIG. 3. (a,b) Snapshots corresponding to a single realization of the steady state for $\phi = 0.064$ at persistence times $\tau_p^{(1)} = 10$ (a) and $\tau_p^{(2)} = 100$ (b), respectively.

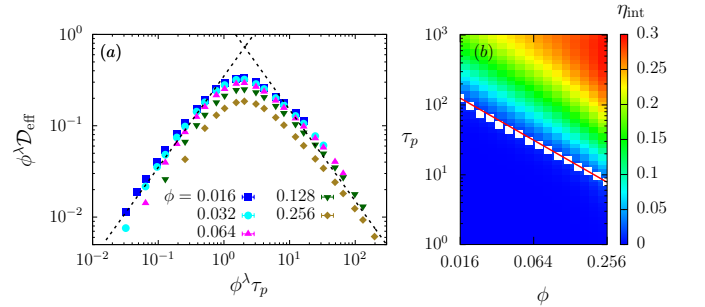


FIG. 4. (a) Scaling collapse plot showing re-scaled effective diffusion coefficient as a function of re-scaled persistence time. The exponent $\lambda \approx 1$ was chosen to yield the best scaling of the data. (b) Density plot of the fraction of particles in the deep interior of a cluster as a function of density and persistence time. White squares represent a numerical calculation of the optimal persistence time at each density, and the solid red line is a best fit using Eq. (3).

the effect of closed tracks is in a sense similar to steric interactions due to other particles, and that dependence of transport on τ_h should be similar to the dependence on ϕ . We will show that this is not always the case: Unlike the density case, the optimal persistence time τ_p^* increases with τ_h .

Figures 5a and 5b show the effective diffusion coeffi-

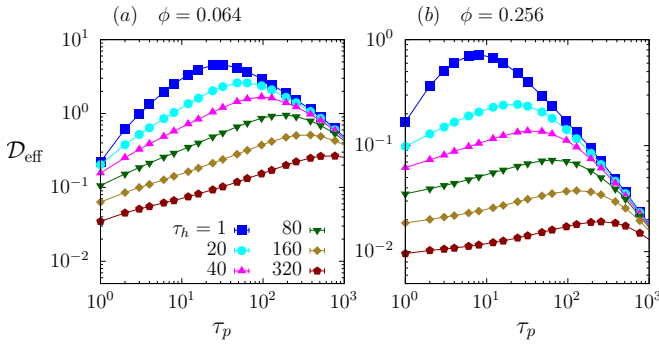


FIG. 5. Effective diffusion coefficient as a function of persistence time for packing fractions $\phi = 0.064$ (a) and $\phi = 0.256$ (b), and several values of the healing time τ_h .

cient as a function of persistence time for several values of τ_h and fixed packing fractions $\phi = 0.064$, and $\phi = 0.256$, respectively. As expected, we observe an overall decrease of D_{eff} with the increase of τ_h . Also, we observe similar qualitative behavior of each $\tau_p \times D_{\text{eff}}$ curve for fixed τ_h in Fig. 5a-b and for fixed ϕ in Fig. 2a. There is an initial increase of D_{eff} with τ_p at low τ_p , which now shows deviations from linear behavior at both high τ_h and high ϕ . At intermediate values of τ_p , D_{eff} reaches a maximum, and then starts decreasing as τ_p^{-1} at high $\tau_p \gg \tau_h$. In fact, we will check that the dominant blocking mechanism for a particle in the regime $\tau_p \gg \tau_h$ is the steric repulsion due to agglomeration, which explains why D_{eff} does not depend on τ_h in this regime. More surprisingly, in contrast with the behavior we have described for fixed topology and varying density [21], the optimal persistence time τ_p^* increases with τ_h . To explain this counterintuitive behavior, we need to take a closer look into the two different mechanisms for particle blocking (the diffusion brakes) in this model.

First, let us note that unlike the fixed topology case ($\tau_h = 1$), for $\tau_h > 1$ there are two blocking mechanisms: (i) Blocking by particles, and (ii) blocking by closed tracks. Crucially, mechanisms (i) and (ii) lead to different behaviors upon increasing τ_p . In Section IV A we have described mechanism (i) in detail. We have argued that the non-monotonic dependence of D_{eff} on τ_p is largely connected with the onset of a finite population of particles in the deep interior of clusters. Upon increasing τ_p , active particles diffuse more in the low persistence regime, but less in the high persistence regime due to agglomeration—particles in the deep interior of a cluster will be more strongly trapped the larger the τ_p . This does not happen for mechanism (ii). As we show in Appendix A, if we turn off steric repulsive interactions (by allowing more than one particle per site), we observe that the effective diffusion coefficient always increases with persistence time. Upon increasing τ_h , it is the redistribution of blocking mechanisms that is ultimately responsible for the “anomalous” increase of τ_p^* with healing time.

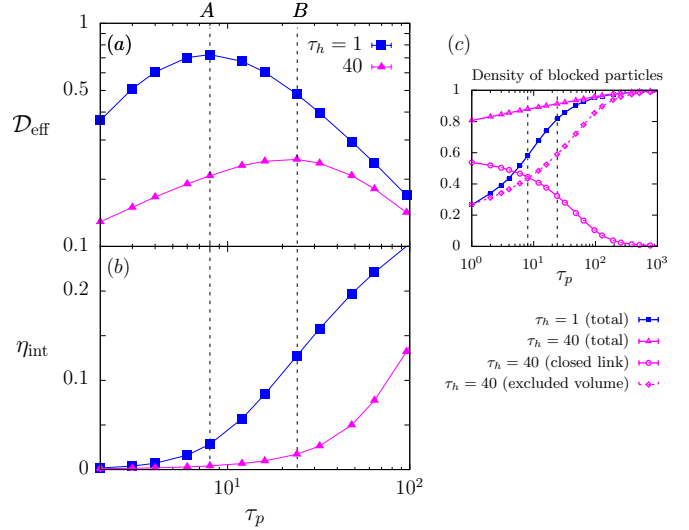


FIG. 6. (a)-(b): Effective diffusion coefficient (a) and fraction of particles in the deep interior of a cluster (b) as a function of persistence time for packing fraction $\phi = 0.256$, and healing times $\tau_h = 1$ and $\tau_h = 40$. The dashed lines A and B indicate the optimal persistence time for each healing time. (c) Density of blocked particles as a function of the persistence time.

Figure 6a shows the effective diffusion coefficient for fixed density $\phi = 0.256$, and healing times $\tau_h = 1$ (no closed bonds) and $\tau_h = 40$ (with closed bonds). Let us consider $\tau_p = \tau_p^{(A)}$, i.e. line A corresponding to τ_p^* when $\tau_h = 1$. As expected, D_{eff} decreases with τ_h due to the introduction of blocking mechanism (ii). In turn, the fraction of particles in the deep interior of a cluster η_{int} also decreases, as shown in Fig. 6b. Since we have observed that it is this population that is responsible for reducing diffusion at large persistence times [as D_{eff} always increases with τ_p for mechanism (ii)], the optimal persistence time for $\tau_h > 1$ has to be located at a value $\tau_h^{(B)} > \tau_h^{(A)}$, thus explaining the observed increase of the optimal persistence time with healing time.

At sufficiently large persistence time, particles organize themselves into larger clusters, and mechanism (i) becomes dominant. Figure 6c shows the fraction of blocked particles as a function of persistence time for $\tau_h = 1$ and $\tau_h = 40$. For $\tau_h = 1$ there is only one mechanism, whereas for $\tau_h = 40$ we show the fraction of blocked particles for each mechanism as well as the total fraction. The dashed lines correspond to lines A and B in Fig. 6a-b. Notice that for large τ_p , almost all blocked particles are due to excluded volume interactions. This explains how the effective diffusion coefficient becomes independent of healing time at large persistence time.

The main results of this section are summarized in the three-dimensional plot shown in Fig. 7, in terms of optimal persistence time, packing fraction and healing time. For points below and above the surface, the effective diffusion coefficient increases and decreases with persistence

time, respectively. Although the optimal persistence time decreases with packing fraction, it increases with healing time, due to the different blocking mechanisms associated with excluded volume and closed tracks. The surface is colored according to the value of the effective diffusion constant at the optimum for each packing fraction and healing time.

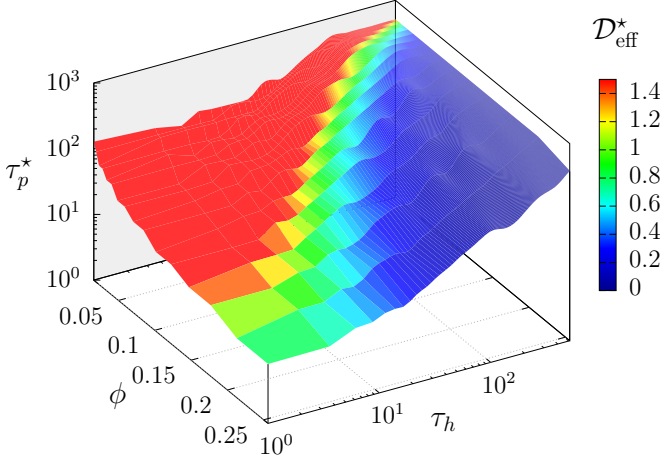


FIG. 7. Optimal persistence time as a function of packing fraction and ‘healing’ time, separating regimes where diffusion increases (below τ_p) and decreases (above τ_p) with persistence time. The color in the surface corresponds to the value of the effective diffusion coefficient at the optimum.

V. CONCLUSIONS

We now make some concluding remarks about our paper. Here we have introduced and investigated transport properties of a model of active particles moving in an adjustable network. In our model, particles move along bonds connecting nearest-neighbor sites of a network, and execute a traditional discrete-version of run-and-tumble motion characterized by a persistence time τ_p . As each particle moves, it leaves a trail of closed links that cannot be used by itself nor by other particles. This trail re-opens, or heals, after a characteristic healing time τ_h . Particles also interact directly via excluded-volume interactions. We find that particle-particle interactions (particles blocked by excluded volume) and particle-network interactions (particles blocked by closed tracks) lead to different diffusive behavior as persistence time is varied. In the limit of no network topology change (i.e. no closed bonds), we recover the expected non-monotonic dependence of the diffusion coefficient on persistence time, with a characteristic increase and decrease at low and high persistencies, respectively. We also use simple scaling arguments to describe these regimes. When we allow network topology changes ($\tau_h > 1$ in our units), we find that the two blocking mechanisms (particle-particle and particle-network interactions) lead to different behaviors

for optimal diffusion in these systems. As a result, the optimal persistence time decreases with density, but increases with healing time. We expect either our model or simple variants of it will be relevant in the description of transport properties of a broad variety of systems of active matter moving in adjustable media, such as self-propelled swimmers in microfluidic devices, slime mold *Physarum polycephalum* and fibroblasts on cartilage tissues.

ACKNOWLEDGMENTS

The authors thank Prof. André Vieira for providing access to his GPU computing resources. The authors also thank Profs. Itai Cohen, James Sethna, Jennifer Schwartz, M. Lisa Manning and Rodrigo Soto for valuable discussions. W.G.C.O. acknowledges support from FAPESP under Grant No. 2024/23876-3. P.d.C. acknowledges financial support from FAPESP under Grants No. 2021/10139-2 and No. 2022/13872-5. H.L. acknowledges support from the German Research Foundation DFG within the project LO418/29-1. D.B.L. acknowledges support from FAPESP under Grants No. 2021/14285-3, No. 2022/09615-7 and No. 2023/14815-8.

Appendix A: Model without steric interactions

To isolate the effect to network topological rearrangements on particle transport, we consider a simplified model with no steric interactions between particles. This allows us to suppress the clustering-induced blocking mechanism and focus exclusively on the impact of closed tracks on transport properties of our model.

Except for a few important differences, the model is essentially the same as the one described in Sec. II. Now the occupation variable of lattice site i has to allow for multiple particles, so that $\sigma_i \in \{0, \dots, N_p\}$. Coordinates x_α for particles α are no longer constrained to be distinct. All the remaining degrees of freedom — namely the bond variables κ_{il} and the self-propulsion directions n_α — are left unchanged. The dynamical rules are modified accordingly. The run-and-tumble dynamics is now free from steric blocking, while the bond-closing and healing processes are implemented exactly as in the original model.

In this simplified setting, where blocking due to particle-particle interactions is absent, we find that the blocking mechanism associated with closed bonds does not give rise to a non-monotonic dependence on τ_p . Instead, we find that increasing τ_p always enhances transport, and D_{eff} increases monotonically for all values of τ_h . We demonstrate this behavior in Fig. 8a and 8b, which show the effective diffusion coefficient is shown as a function of τ_p for different values of τ_h and fixed packing fractions $\phi = 0.016$ (a) and $\phi = 0.256$ (b), respectively.

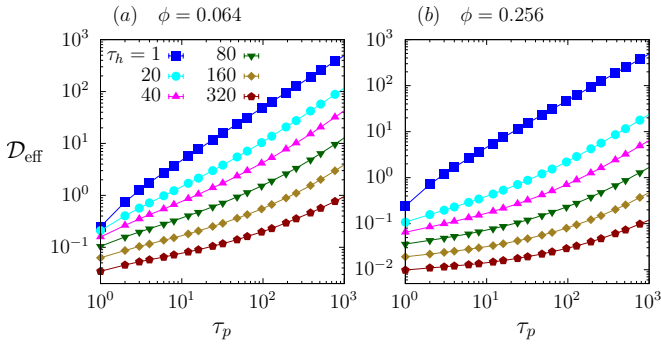


FIG. 8. Effective diffusion coefficient as a function of the persistence time for different healing times, at packing fractions $\phi = 0.064$ (a) and $\phi = 0.256$ (b). In this model, steric interactions are absent.

[1] S. Ramaswamy, The mechanics and statistics of active matter, *Annu. Rev. Condens. Matter Phys.* **1**, 323 (2010).

[2] M. C. Marchetti, J.-F. Joanny, S. Ramaswamy, T. B. Liverpool, J. Prost, M. Rao, and R. A. Simha, Hydrodynamics of soft active matter, *Reviews of modern physics* **85**, 1143 (2013).

[3] J. Elgeti, R. G. Winkler, and G. Gompper, Physics of microswimmers—single particle motion and collective behavior: a review, *Reports on progress in physics* **78**, 056601 (2015).

[4] C. Bechinger, R. Di Leonardo, H. Löwen, C. Reichhardt, G. Volpe, and G. Volpe, Active particles in complex and crowded environments, *Reviews of modern physics* **88**, 045006 (2016).

[5] M. Te Vrugt and R. Wittkowski, Metareview: a survey of active matter reviews, *The European Physical Journal E* **48**, 12 (2025).

[6] G. Gompper, R. G. Winkler, T. Speck, A. Solon, C. Nardini, F. Peruani, H. Löwen, R. Golestanian, U. B. Kaupp, L. Alvarez, *et al.*, The 2020 motile active matter roadmap, *Journal of Physics: Condensed Matter* **32**, 193001 (2020).

[7] M. te Vrugt, B. Liebchen, and M. E. Cates, What exactly is ‘active matter’? (2025), arXiv:2507.21621 [cond-mat.soft].

[8] F. Sagués Mestre, *Colloidal Active Matter: Concepts, Experimental Realizations, and Models* (CRC Press, 2022).

[9] A. Escobar, R. Reyes-Aguilar, C. Vidales-Hernández, J. Carrillo-Estrada, and F. Donado, Effect of particle concentration on the persistence of motion in active matter systems, *Physica A: Statistical Mechanics and its Applications* **659**, 130344 (2025).

[10] E. Agoritsas and P. K. Morse, Memory formation in dense persistent active matter (2024), arXiv:2403.11701 [cond-mat.soft].

[11] H. H. Wensink and H. Löwen, Aggregation of self-propelled colloidal rods near confining walls, *Phys. Rev. E* **78**, 031409 (2008).

[12] I. Theurkauff, C. Cottin-Bizonne, J. Palacci, C. Ybert, and L. Bocquet, Dynamic clustering in active colloidal suspensions with chemical signaling, *Physical review letters* **108**, 268303 (2012).

[13] L. Caprini, D. Breoni, A. Ldov, C. Scholz, and H. Löwen, Dynamical clustering and wetting phenomena in inertial active matter, *Communications Physics* **7**, 343 (2024).

[14] S. Lévy, A. Katona, H. Löwen, R. Cruz Hidalgo, and I. Zuriguel, Cluster dynamics in macroscopic photoactive particles, *Physical Review Letters* **135**, 098301 (2025).

[15] M. E. Cates and J. Tailleur, Motility-induced phase separation, *Annu. Rev. Condens. Matter Phys.* **6**, 219 (2015).

[16] J. Palacci, S. Sacanna, A. P. Steinberg, D. J. Pine, and P. M. Chaikin, Living crystals of light-activated colloidal surfers, *Science* **339**, 936 (2013).

[17] I. Buttinoni, J. Bialké, F. Kümmel, H. Löwen, C. Bechinger, and T. Speck, Dynamical clustering and phase separation in suspensions of self-propelled colloidal particles, *Phys. Rev. Lett.* **110**, 238301 (2013).

[18] C. Kurzthaler, S. Mandal, T. Bhattacharjee, H. Löwen, S. S. Datta, and H. A. Stone, A geometric criterion for the optimal spreading of active polymers in porous media, *Nature communications* **12**, 7088 (2021).

[19] V. E. Debets, X. M. De Wit, and L. M. Janssen, Cage length controls the nonmonotonic dynamics of active glassy matter, *Physical Review Letters* **127**, 278002 (2021).

[20] K. Martens, L. Angelani, R. Di Leonardo, and L. Bocquet, Probability distributions for the run-and-tumble bacterial dynamics: An analogy to the lorentz model, *The European Physical Journal E* **35**, 84 (2012).

[21] D. Levis and L. Berthier, Clustering and heterogeneous dynamics in a kinetic monte carlo model of self-propelled hard disks, *Phys. Rev. E* **89**, 062301 (2014).

[22] R. Soto and R. Golestanian, Run-and-tumble dynamics in a crowded environment: Persistent exclusion process for swimmers, *Phys. Rev. E* **89**, 012706 (2014).

[23] A. P. Solon and J. Tailleur, Flocking with discrete symmetry: The two-dimensional active ising model, *Physical Review E* **92**, 042119 (2015).

[24] M. Scandolo, J. Pausch, and M. E. Cates, Active ising models of flocking: a field-theoretic approach, *The European Physical Journal E* **46**, 103 (2023).

[25] S. Bandyopadhyay, S. Chatterjee, A. K. Dutta, M. Karimkar, H. Rieger, and R. Paul, Ordering kinetics in the active ising model, *Physical Review E* **109**, 064143

(2024).

[26] F. Dittrich, T. Speck, and P. Virnau, Critical behavior in active lattice models of motility-induced phase separation, *The European Physical Journal E* **44**, 53 (2021).

[27] S. A. Loos, S. H. Klapp, and T. Martynec, Long-range order and directional defect propagation in the nonreciprocal xy model with vision cone interactions, *Physical review letters* **130**, 198301 (2023).

[28] C. Jin, C. Krieger, and C. C. Maass, Chemotaxis and autochemotaxis of self-propelling droplet swimmers, *Proceedings of the National Academy of Sciences* **114**, 5089 (2017).

[29] D. Bi, J. Lopez, J. M. Schwarz, and M. L. Manning, A density-independent rigidity transition in biological tissues, *Nature Physics* **11**, 1074 (2015).

[30] D. Bi, X. Yang, M. C. Marchetti, and M. L. Manning, Motility-driven glass and jamming transitions in biological tissues, *Phys. Rev. X* **6**, 021011 (2016).

[31] C. P. Goodrich, A. J. Liu, and S. R. Nagel, The principle of independent bond-level response: Tuning by pruning to exploit disorder for global behavior, *Phys. Rev. Lett.* **114**, 225501 (2015).

[32] D. R. Reid, N. Pashine, J. M. Wozniak, H. M. Jaeger, A. J. Liu, S. R. Nagel, and J. J. de Pablo, Auxetic metamaterials from disordered networks, *Proceedings of the National Academy of Sciences* **115**, E1384 (2018), <https://www.pnas.org/doi/pdf/10.1073/pnas.1717442115>.

[33] D. B. Liarte, O. Stenull, and T. C. Lubensky, Multi-functional twisted kagome lattices: Tuning by pruning mechanical metamaterials, *Phys. Rev. E* **101**, 063001 (2020).

[34] J. W. Rocks, N. Pashine, I. Bischofberger, C. P. Goodrich, A. J. Liu, and S. R. Nagel, Designing allosteric-inspired response in mechanical networks, *Proceedings of the National Academy of Sciences* **114**, 2520 (2017), <https://www.pnas.org/doi/pdf/10.1073/pnas.1612139114>.

[35] J. W. Rocks, H. Ronellenfitsch, A. J. Liu, S. R. Nagel, and E. Katifori, Limits of multifunctionality in tunable networks, *Proceedings of the National Academy of Sciences* **116**, 2506 (2019), <https://www.pnas.org/doi/pdf/10.1073/pnas.1806790116>.

[36] M. Stern, D. Hexner, J. W. Rocks, and A. J. Liu, Supervised learning in physical networks: From machine learning to learning machines, *Phys. Rev. X* **11**, 021045 (2021).

[37] V. F. Hagh, S. R. Nagel, A. J. Liu, M. L. Manning, and E. I. Corwin, Transient learning degrees of freedom for introducing function in materials, *Proceedings of the National Academy of Sciences* **119**, e2117622119 (2022), <https://www.pnas.org/doi/pdf/10.1073/pnas.2117622119>.

[38] S. Dillavou, B. D. Beyer, M. Stern, A. J. Liu, M. Z. Miskin, and D. J. Durian, Machine learning without a processor: Emergent learning in a nonlinear analog network, *Proceedings of the National Academy of Sciences* **121**, e2319718121 (2024), <https://www.pnas.org/doi/pdf/10.1073/pnas.2319718121>.

[39] T. Hain, C. Santangelo, and M. L. Manning, Optimizing properties on the critical rigidity manifold of under-constrained central-force networks, *Phys. Rev. E* **111**, 015418 (2025).

[40] M. Stern and A. Murugan, Learning without neurons in physical systems, *Annual Review of Condensed Matter Physics* **14**, 417 (2023).

[41] L. Tröger, F. Goirand, and K. Alim, Size-dependent self-avoidance enables superdiffusive migration in macroscopic unicellulars, *Proceedings of the National Academy of Sciences* **121**, e2312611121 (2024), <https://www.pnas.org/doi/pdf/10.1073/pnas.2312611121>.

[42] J. L. Silverberg, A. R. Barrett, M. Das, P. B. Petersen, L. J. Bonassar, and I. Cohen, Structure-function relations and rigidity percolation in the shear properties of articular cartilage, *Biophysical journal* **107**, 1721 (2014).

[43] T. W. Jackson, J. Michel, P. Lwin, L. A. Fortier, M. Das, L. J. Bonassar, and I. Cohen, Structural origins of cartilage shear mechanics, *Science Advances* **8**, eabk2805 (2022), <https://www.science.org/doi/pdf/10.1126/sciadv.abk2805>.

[44] Alternative lattice geometries, including square and honeycomb lattices, yield the same qualitative phenomenology.

[45] G. Bandini, D. Venturelli, S. A. Loos, A. Jelic, and A. Gambassi, The xy model with vision cone: nonreciprocal vs. reciprocal interactions, *Journal of Statistical Mechanics: Theory and Experiment* **2025**, 053205 (2025).

[46] Y. Avni, M. Fruchart, D. Martin, D. Seara, and V. Vitelli, Nonreciprocal ising model, *Physical Review Letters* **134**, 117103 (2025).

[47] D. Martin, D. Seara, Y. Avni, M. Fruchart, and V. Vitelli, Transition to collective motion in nonreciprocal active matter: Coarse graining agent-based models into fluctuating hydrodynamics, *Physical Review X* **15**, 041015 (2025).

[48] R. Khasseh, S. Wald, R. Moessner, C. A. Weber, and M. Heyl, Active quantum flocks, *Physical Review Letters* **135**, 248302 (2025).

[49] J. Sanders and E. Kandrot, *CUDA by example: an introduction to general-purpose GPU programming* (Addison-Wesley Professional, 2010).

[50] NVIDIA, CUDA toolkit documentation (2026).

[51] M. F. Sykes and J. W. Essam, Exact critical percolation probabilities for site and bond problems in two dimensions, *Journal of Mathematical Physics* **5**, 1117 (1964).